



ORIGINAL ARTICLE-BASIC SCIENCE OPEN ACCESS

Potential of Heparan Sulphate Mimetics Integrated Into Collagen Scaffolds for Enhanced Skin Wound Healing

¹Radboud university medical center, Research Institute for Medical Innovation, Department of Medical BioSciences, Nijmegen, the Netherlands | ²OTR3, Paris, France | ³LUMC, Department of Immunology, Leiden, the Netherlands | ⁴Alliance of Dutch Burn Care, Burn Research Lab, Beverwijk, the Netherlands | ⁵Department of Plastic, Reconstructive and Hand Surgery, AUMC, Amsterdam, the Netherlands

Correspondence: Willeke F. Daamen (willeke.daamen@radboudumc.nl)

Received: 1 May 2025 | Revised: 10 September 2025 | Accepted: 25 September 2025

Funding: This work was supported by European Union's Horizon 2020 research and innovation programme under the Marie Skłodowska-Curie Grant Agreement No. 955722 (SkinTERM, NAM, RK) and from Radboud university medical center PhD round 2020 PI and MSc competition, respectively (MG and MP).

Keywords: biomaterials | macrophages | OTR4120 | rat model | sonic hedgehog

ABSTRACT

Optimal healing of full-thickness skin wounds remains a clinical challenge. While current skin substitutes aid burn wound management, there is still a need to effectively minimize scarring. Therefore, we developed type I collagen scaffolds with covalently bound ReGeneraTing Agent (RGTA) OTR4120 (OTR), a synthetic heparan sulphate analogue resistant to glycanase degradation (Col I+OTR). To further stimulate skin regeneration, collagen scaffolds with and without OTR4120 were subsequently loaded with sonic hedgehog (SHH), a key effector molecule in embryogenesis. The presence of OTR4120 and SHH in scaffolds was biochemically and histologically confirmed after crosslinking and sterilization. SHH was found deeper into collagen scaffolds in the presence of OTR4120. Addition of SHH to scaffolds showed lower expression of M1-like cell surface markers, while Col I+OTR significantly enhanced IL-10 production. The potential of OTR4120 in wound healing was further evaluated in vivo using a rat full-thickness wound model over 28 days. By day 14, macroscopic images revealed that OTR-treated wounds better maintained the original wound shape. Histological analysis showed increased blood vessel formation, fewer scaffold remnants and more contiguous sebaceous glands in the granulation tissue with Col I+OTR scaffolds. This study demonstrates that OTR4120 could be a promising addition to acellular skin substitutes for improving acute wound healing.

1 | Introduction

Deep and extensive injuries, such as burns, often lead to significant scarring, which can cause contraction and mobility limitations for patients [1]. Full-thickness skin wounds compromise the integrity of the epidermis and dermis, including appendages, creating a need for skin replacement to avoid complications [2].

The gold standard treatment for this type of wound involves split-thickness skin transplants [3]. However, this method not only creates an additional superficial wound in the patient but can also lead to incomplete skin repair, often resulting in fibrotic tissue [4]. Dermal templates, such as collagen scaffolds, can provide structural support for dermal restoration during the wound healing process [5, 6].

This is an open access article under the terms of the Creative Commons Attribution-NonCommercial License, which permits use, distribution and reproduction in any medium, provided the original work is properly cited and is not used for commercial purposes.

© 2025 The Author(s). Wound Repair and Regeneration published by Wiley Periodicals LLC on behalf of The Wound Healing Society.

Wound healing stages consist of overlapping phases: haemostasis, inflammation, proliferation and remodelling [7]. Haemostasis initiates wound healing by rapidly constricting blood vessels, forming a fibrin clot to stop bleeding and releasing signalling molecules that recruit immune cells [8]. During inflammation, monocyte-derived macrophages (M0) arrive at the wound site and polarize toward M1 (proinflammatory) macrophages to remove debris and pathogens, which are replaced by M2 (pro-healing) macrophages that help resolve inflammation and signal the start of proliferation [9-11]. During this phase, fibroblasts transform into myofibroblasts and secrete extracellular matrix (ECM) components to form granulation tissue and contract the wound, while endothelial cells promote angiogenesis to support tissue growth [12]. Fast wound contraction during the skin healing process usually leads to scarring [13]. Keratinocytes cover the wound and the provisional ECM is degraded to allow tissue reconstruction [14], while (myo)fibroblasts deposit type I collagen [15].

One way to improve the function of dermal templates is through biofunctionalization with molecules present in the ECM. Several studies described incorporating heparin in collagen scaffolds for its potential to bind growth factors, which can enhance skin wound healing [16, 17]. However, after an injury the environment is characterized by a catabolic activity leading to a rapid degradation of heparan sulphate and other molecules [18]. To tackle this, dextran-derived analogues, such as ReGeneraTing Agents (RGTA), have been developed to mimic the structural and functional properties of heparan sulphate but are resistant to degradation by heparanases, chondroitinases, hyaluronidase and dextranase [19, 20], due to the presence of 1-6 bonds between the monosaccharides instead of the natural 1–4 glycosidic bonds in heparan sulphates [21]. We therefore decided to construct collagen scaffolds with RGTA OTR4120 (OTR) to evaluate its potential as a dermal template in acute wounds.

Effector molecules are essential for ECM signalling during wound healing [22]. Sonic hedgehog (SHH) is a key regulator in the hedgehog pathway that influences tissue formation, hair follicle development, cell fate and epidermal patterning during embryogenesis [23]. Higher SHH expression has been observed in embryonic mice with regenerated wounds compared to older mice that developed scars [24, 25]. Sulphation of heparan sulphate is crucial for SHH binding, as a study demonstrated SHH dimers assemble on heparin chains with three sulphate groups per disaccharide [26]. The formed complex enhances SHH bioavailability, a principle that can be applied in scaffolds. Moreover, SHH has shown to act as a chemoattractant for macrophages in vivo [27]. The incorporation of SHH and OTR4120 in collagen scaffolds may thus impact macrophage polarization. Recently, our research group described an antifibrotic effect of type I collagen scaffolds functionalized with OTR4120 in combination with FGF2 in an in vitro model using fibroblasts [28]. In this study, we evaluate the binding capacity of OTR4120 for SHH in collagen scaffolds, as well as its effect on macrophages in vitro. The wound healing potential of OTR4120 bound to collagen scaffolds is further evaluated in vivo using a rat full-thickness wound model.

2 | Materials and Methods

2.1 | Scaffold Construction and Characterization

Porous collagen scaffolds (Col I) were prepared using 0.8% (w/v) collagen fibrils in 0.25 M acetic acid, swollen overnight at 4°C under constant agitation. The collagen was isolated from bovine Achilles tendon obtained from a local slaughterhouse [29]. For collagen scaffolds with RGTA OTR4120 (Col I+OTR), 0.025 (w/v) % of heparan sulphate mimetic (OTR3, Paris, FR) [30] was added to the 0.8% (w/v) collagen suspension. The suspensions were homogenized and poured into standard suspension culture plates (6-well format, Cellstar, Greiner Bio-One, cat. no. 657185) at 4mL per well (corresponding to 960 mm² surface area per well). The plates were then frozen at −20°C before lyophilization using a Lyoph-pride 03 freeze dryer (ilShin BioBase Europe, Ede, NL), creating untreated non-crosslinked scaffolds (U). Scaffolds for characterization, in vitro and in vivo testing were chemically crosslinked (X) for 3 h, applying 33 mM 1-ethy 1-3-(3-dimethylaminopropyl)-carbodiimide (EDC) and 6 mM Nhydroxysuccinimide (NHS) in 50 mM 2-morpholinoethane sulphonic acid (MES, pH 5.0) (Sigma-Aldrich, St. Louis, MO, USA) containing 40% ethanol. Scaffolds were washed with 0.1 M Na₂HPO₄, 1M NaCl, 2M NaCl and demineralized water, and lyophilized. Finally, Ø 12-mm scaffolds were gamma sterilized (Steris company, Ede, NL) with a minimum dose of 25 kGy.

Col I+OTR/SHH scaffolds were prepared by incubating dry Col I+OTR scaffolds in $3.5\,\mu\text{g/mL}$ human SHH C24II (Lot. 5,221,207,908, SHH, Miltenyi Biotec, Teterow, DE) in phosphate buffered saline (PBS, pH7.2) overnight. Scaffolds without OTR4120 (Col I+SHH) were used as a control for characterization. Scaffolds were washed $3\times15\,\text{min}$ in PBS to remove unbound SHH and processed for further analysis. Samples for in vitro studies were used immediately. Samples for characterization, including the supernatants from the washing steps, were stored either in sample buffer (1.0% w/v sodium dodecyl sulphate (SDS), 1.25% v/v 2-mercaptoethanol, 2.5% v/v glycerol and 0.04% w/v bromophenol blue in 31.25 mM Tris–HCl in Milli-Q water) at $-20\,^{\circ}\text{C}$ or in Tissue-Tek O.C.T. compound (Sakura Finetek, Alphen aan den Rijn, NL) at $-80\,^{\circ}\text{C}$.

The extent of crosslinking was evaluated by measuring the residual primary amine groups through 2,4,6-trinitrobenzene sulphonic acid (TNBS) assay [31]. Glycine solutions (0–80 $\mu g/mL$) prepared in 4% NaHCO $_3$ were used for calibration, and absorbance was measured at 420 nm using a SpectraMax iD3 plate reader (Molecular Devices, CA, USA). The pore structure of the scaffolds was visualized using scanning electron microscopy (SEM). In short, the cross-sectional side of the scaffolds was attached to carbon tape, coated with gold in an Edwards Scancoat Six Sputter Coater (Crawley, UK) and imaged with a Zeiss Sigma 300 SEM (Jena, DE) at 3 kV.

The amount of OTR4120 bound to the scaffolds was determined by performing a dot blot colorimetric assay with Alcian blue staining. Scaffolds were digested at 65°C overnight using 2.5 U/mL papain (P3125, Merck, Darmstadt, DE) in 50 mM sodium phosphate, 2 mM EDTA, and cysteine (pH6.5). The samples were spotted on a polyvinylidene fluoride membrane

(0.45 µm, Thermo Scientific, Waltham, MA, USA) activated with 0.25 (w/v) % cetylpyridinium chloride (CPC) in methanol with 30% isopropanol alongside a serial dilution of OTR4120 starting from 500 ng. Alcian blue staining solution contained 2.5 (w/v) % Alcian blue (Sigma) in de-staining solution (40 mM guanidinium chloride, $1.8\,\text{mM}$ H_2SO_4 , and $0.025\,\text{v/v}$ % Triton X-100 in 50% aqueous ethanol). Membranes were stained for 30 min in Alcian blue solution, followed by a 5 min incubation in de-staining solution and 5 min in demineralized water [32]. Membranes were imaged with the Molecular Imager Gel Doc XR system (Bio-Rad) on a White Light Conversion Screen (Bio-Rad, Hercules, CA, USA) in grayscale. The OTR4120 content of the samples was measured as μg OTR4120/mg collagen.

2.2 | SHH Quantification and Localization

The amount of SHH bound to the scaffolds was measured using Western blotting. Samples and SHH for the calibration curve in sample buffer were boiled for 10 min. Samples, including a Protein Ladder (PageRuler Plus, Thermo Scientific), were run on a 12% SDS-PAGE gel for 1.5 h at 100 V. Proteins on the gel were blotted onto a nitrocellulose membrane (0.2 µm, Bio-Rad) at 100 V for 1 h in blotting buffer (25 mM Tris, 40 mM glycine, in 20% aqueous methanol with 0.4% SDS). Membranes were blocked with 2% bovine serum albumin (BSA) in PBST (0.1% Tween-20 in PBS) overnight at 4°C under constant agitation. Immunostaining was performed by incubating the membrane with rabbit anti-human SHH (1:5000, sc-9024 Santa Cruz Biotechnology, Dallas, TX, USA) for 1 h, followed by goat anti-rabbit IRDye 680 CW conjugated (1:5000, 929-32,221, Li-COR Biotechnology, Lincoln, NE, USA) for 1 h. Blots were washed with PBST for 3×5min between antibody incubations. Blots were scanned using the Odyssey CLx imager (Li-COR), and the signal was quantified using Image Studio Version 6.0 (LI-COR).

The distribution of OTR4120 and SHH was visualized using indirect fluorescence microscopy. Then, 7-µm cryosections of scaffold cross-sections were blocked with 2% BSA in PBST for 30 min. All antibodies were diluted in blocking solution (BSA-PBST) and left for incubation for 1h, followed by washes of PBST 3×5min between labelling steps. Three antibodies were used to stain OTR4120: primary single chain antibody HS4C3V with a VSV tag (1:10 periplasmic fraction, produced in house), secondary mouse anti-VSV P5D4 hybridoma supernatant (1:10, produced in house), [33], tertiary goat anti-mouse IgG (H+L) Alexa 488 conjugated (1:500, A-11001, Molecular Probes Inc). To visualize SHH, anti-rabbit SHH (1:100, Santa Cruz) was used, followed by secondary goat anti-rabbit IgG (H+L) Alexa 594 conjugated (1:500, A-11012, Molecular Probes Inc). Slides were fixated in absolute ethanol and mounted with Mowiol 4-88 (Merck). Images were taken using ZOE Fluorescence Cell Imager (Bio-Rad).

2.3 | In Vitro Analysis With Human Macrophages

Primary human monocytes were isolated from peripheral blood mononuclear cells of healthy donors (3 donors), using magnetic activated beads, CD14⁺ (130–050-201, Miltenyi Biotech, Teterow,

DE). Each donor was tested in an independent experiment performed at separate times. Informed consent was given in accordance with the Declaration of Helsinki and Dutch national and Sanguin internal ethic boards. Monocytes were stimulated with 50 ng/mL macrophage colony-stimulating factor (M-CSF, PeproTech by Thermo Scientific, Waltham, MA, USA) for 6 days to obtain M0 macrophages. As controls, M0 macrophages were stimulated for 24h with 100 ng/mL lipopolysaccharides (LPS, vac-3pelps, InvivoGen, San Diego, CA, USA) with 20 ng/mL interferon gamma (IFNy, PeproTech) to polarize them to M1-like macrophages or with 20 ng/mL interleukin 4 (IL4, 170-076-135) + 20 ng/mL interleukin 13 (IL13, 130-112-412) to polarize them to M2-like macrophages (both from Miltenyi Biotech). On day 7, cells were harvested with a cell scraper using 2 mM EDTA in PBS. In total, 200,000M0 macrophages were seeded onto crosslinked collagen-based scaffolds, which included the following experimental conditions: Col I (control), Col I + OTR and Col I+OTR/SHH. As additional controls, Col I scaffolds were also seeded with either M1- or M2-like macrophages that were pre-differentiated. Macrophages were cultured on scaffolds for 48h in RPMI 1640 medium containing 10% foetal bovine serum (FBS, Gibco), 1% ultraglutamine and 1% antibiotic/antimycotic with their respective stimulators (M0: /; M1: LPS + IFN γ ; M2: IL4+IL13) during the differentiation process and without these factors during scaffold culture.

Cell phenotype was evaluated using flow cytometry. Macrophages were enzymatically retrieved from the scaffolds using 0.25 U/mL collagenase A (Roche, Mannheim, DE) in a shaking water bath for 30 min at 37°C. PBS containing EDTA was added to the scaffolds and incubated for 30 min at 4°C. Isolated cells were labelled with eFluor 780-APC-Cy7 (1:2000, 65-0865-14, ThermoFisher, Carlsbad, CA, USA) to detect viable cells. For cell surface labelling, antibodies were used from either BD Biosciences (Franklin Lakes, NJ, USA) or BioLegend (San Diego, CA, USA) and corresponded to CD45 (1:20, 304,026), CD80 (1:20, 305,220), PD-L1 (1:30, 557,924), HLA-DR (1:20, 307,646), CD206 (1:40, 551,135), CD163 (1:40, 562,643) and MerTK (1:50, 367,610). Mean fluorescence intensity (MFI) was measured with BD FACSVerse Cell Analyser flow cytometer (BD BioSciences) and calculated using FlowJo X (vX 0.7, Tree STAR, Ashland, OR, USA). Gating strategy consisted of spotting singlet live cells, CD45+cells, and a specific CD marker.

Cytokine concentrations in supernatants were quantified using ELISA kits for IL-12 (88–7126), IL-6 (88–7066) and IL-10 (88–7106) (Invitrogen, ThermoFisher, Vienna, AT), following the manufacturer's instructions. Absorbances were recorded at 450 nm using the iMark Microplate Absorbance Reader (Bio-Rad, Basel, CH).

2.4 | In Vivo Analysis With Rats

All procedures were performed according to the Institute of Laboratory Animal Research guide for Laboratory Animals. The study was approved by the Ethics Committee of the Radboud University Nijmegen DEC 2023–0016 under the project licence AVD10300202317189. A powered analysis based on a similar approach by Nillesen et al. [16] was performed, taking into account the wound contraction percentage between untreated and collagen-based substitute, calculating a

relevant detectable contrast of 20%. This resulted in a sample size of 9 rats for a power of 80% and alpha = 0.05 (two sided). Nine Wistar rats (male, 3 months old, weight 300–400 g, WI (WU), Charles River) were purchased and housed with two rats per cage. They were fed with pellets, sunflower seeds, booster food (Ssniff Spezialdiäten, Soest, DE) and water *ad libitum*. The rats were labelled by ear punch upon arrival and were handled and trained for a period of 1–2 weeks before surgery.

The experimental design consisted of the following treatment groups: untreated wound, Col I scaffold and Col I+OTR scaffold. Note that the experiment contained another collagen-based condition not related to this study. The treatment location was randomized using randomizator.org to avoid repetitions of sets. Spots were assigned A–D on the back of the rats, and treatments 1–4 were allocated in a different order. Rats were sacrificed at day 28 after implantation (Supporting Information Figure S1).

Rats were anesthetized with isoflurane 1.5%-2.5%. Eye cream (Ophtosan, AST Farma, Oudewater, NL) was applied to their eyes. Their backs were trimmed using a hair clipper and hair removed by applying Veet cream (Reckitt Benckiser, Slough, UK). Four full-thickness wounds of Ø 12 mm were made on the back of each rat, between the shoulders and hind legs using a biopsy punch (220,701, SMI AG, St. Vith, BE) and curved scissors. Sterile scaffolds were placed on the wounds in such a way that they fitted exactly and touched the wound edge. The scaffolds were kept in place using 6-8 resorbable sutures (100L6P, Monocryl 4-0, Ethicon, Raritan, NJ, USA). Wounds were covered with a silicone dressing (Mepilex Border Flex Lite, 581,277, Mölnlycke, Gothenburg, SE), an elastic bandage (PetFlex 10,009,403,914, Andover healthcare, Portsmouth, NH, USA) and adhesive plaster (250, Leukoplast, Hamburg, DE). Post-operative analgesia was given after surgery and for the next 3 days with 0.1 mL/100 g body weight injections of carprofen (5 mg/mL, Rimadyl, Capelle a/d IJssel, NL). Wound dressing and bandaging were replaced when needed, generally 1-3 times per week.

Digital photos of the wounds were taken at days 0, 7, 14, 21 and 28 post surgery, plus when dressings and bandages were changed. Rats were sacrificed on day 28 by CO_2 inhalation, and scaffolds with surrounding tissue were harvested. Half of the tissue was stored in 4% paraformaldehyde (PFA) in PBS overnight and replaced with 1% PFA in PBS thereafter. The other half was snapfrozen in liquid N_2 , stored in TissueTek and frozen at $-80^{\circ}\mathrm{C}$.

2.4.1 | Morphology and Wound Contraction Analysis

Macroscopic images were processed in FIJI 1.53t (ImageJ software, Bethesda, MD, USA) and calibrated using the photographed ruler in each photo to obtain the width, length and wound area by manually tracing the wound edge ($n \le 9$). The morphology was evaluated according to the ratio observed between the width and length of the wound (Supporting Information Figure S2). A morphology closer to 1 represents a rounder wound, which is an indication of less contraction. The formula used was

Morphology (1) =
$$\frac{\text{width (cm)}}{\text{length (cm)}}$$

Wound contraction was evaluated by determination of the remaining wound area using the photographs at the different timepoints (7, 14, 21 and 28 days) compared to day 0 (i.e., 100% of the wound area) per condition. The formula used to calculate the wound contraction was

Wound contraction (%) =
$$\frac{Ai - Ax}{Ai} \cdot 100\%$$

where: Ai = Initial wound area at day 0; Axe = Wound area at the timepoint (i.e., day 7, 14, 21 or 28).

2.4.2 | Microscopical Analysis

Histological analysis: PFA fixed samples were embedded in paraffin and sections of $5\,\mu m$ thickness were cut. Sections were stained with haematoxylin and eosin (H&E) or Masson's trichome blue and scanned with a whole-slide scanner (3DHISTECH, Budapest, HU). CaseViewer 2.4 software was used to analyse the histological sections and immunostainings. The stainings were used to visualize skin layers, appendages and scaffold remnants.

2.4.2.1 | Immunohistochemistry. Samples were stained for alpha smooth muscle actin (α-SMA, 1:2000, clone 1A4, A-2547, Merck) to visualize myofibroblasts and mature blood vessels and for cluster of differentiation 68 (CD68, 1:200, MCA341R, AbD Serotec) to study macrophages. Sections were deparaffinized and incubated with 0.5% hydrogen peroxide (K44653709, Merck) for 1h. After washing with demineralized water for 5 min, the samples were incubated for 10 min in boiling citrate buffer (10 mM tri-sodium citrate, pH 6.0). After cooling for 40 min, sections were rinsed in demineralized water for 2×2min and incubated with blocking solution (0.5% BSA in PBS+0.05% Triton X-100) for 30 min. All antibodies used in this methodology and ABC kit were diluted in blocking solution and washed with PBS 2×5min. Primary antibodies were incubated for 45 min. From this point, reagents were from Vector Laboratories (Newark, CA, USA). Secondary antibody goat anti-mouse IgG (H+L) biotinylated (1:200, BA-9200) was incubated for 45 min. Elite ABC kit, peroxidase (PK-6100) was applied for 1h. AEC substrate kit, peroxidase (SK-4205) was incubated for 5-8 min. Sections were counterstained with haematoxylin and mounted using VectorMount (H-5501).

2.4.2.2 | **Quantitative Measurements.** Using H&E, the epidermal thickness at both the wound and unwounded healthy skin was measured at three different areas. The wound area was marked by the presence of granulation tissue. The number of hair follicles and sebaceous glands was counted within the wound and in the adjacent area. The histological wound deformation was calculated by dividing the width of the middle of the wound by the width of the wound just below the epidermis.

Deformation (1) =
$$\frac{\text{Width from the middle dermis } (\mu m)}{\text{Width from the top dermis } (\mu m)}$$

2.4.2.3 | **Semi-Quantitative Scoring.** The healed tissue was semi-quantitatively scored by two independent individuals (NA, RK) for the presence of myofibroblasts, macrophages,

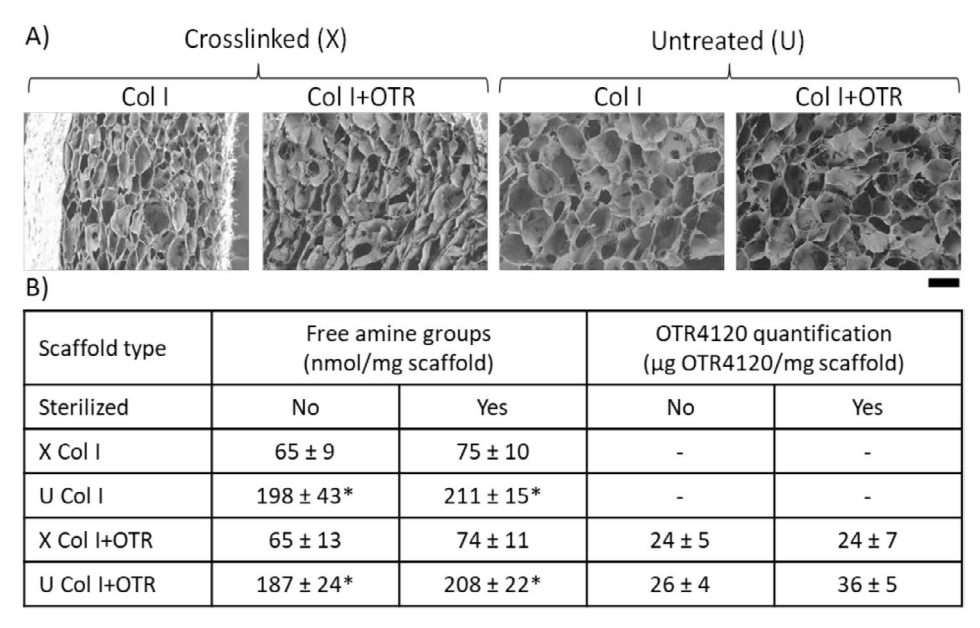


FIGURE 1 | Effect of crosslinking and gamma sterilization of scaffolds. (A) Representative images of the pore morphology in cross-section of crosslinked (X) and untreated (U) collagen scaffolds using scanning electron microscopy. Scale bar is $200 \,\mu\text{m}$. (B) Table displaying the characteristics of Col I scaffolds with and without OTR4120, before and after sterilization. '-' represents below detection limits. N=3 (mean \pm SD). Two-way ANOVA followed by Tukey's multiple comparison test was performed for primary amine groups. *Significant reduction in primary amine group content was observed in crosslinked scaffolds compared to their non-crosslinked counterparts (p < 0.001).

angiogenesis and residual collagen based on AEC and trichrome blue staining. Scores were assigned from 0 (not present) to 1, 2 or 3 (low, medium, high abundance, respectively). If differences occurred between observers (when intra-class correlation coefficient, ICC < 0.75), slides were re-evaluated to obtain consensus.

2.5 | Statistical Analysis

Data were analysed and visualized using GraphPad Prism 10.4.1. Scaffolds characterization and histological analysis from rat tissues were evaluated using one-way ANOVA with Tukey's multiple comparisons test. For in vitro studies and macroscopical analyses of in vivo studies, two-way ANOVA with Tukey's multiple comparison test was performed. Type I error was set at 5% (i.e., α =0.05). IBM SPSS Statistics 29 (Armonk, NY, USA) was used to determine the ICC to evaluate if the reliability was good (>0.75) or excellent (>0.9) between scorers in the histology section (Supporting Information Table S1).

3 | Results

3.1 | Effect of Sterilization and Crosslinking on OTR4120 Bound to Collagen Scaffolds

Porous scaffolds were prepared containing type I collagen (Col I) or type I collagen with 0.025% OTR4120 (Col I+OTR). Scanning electron microscopy images revealed that crosslinked Col I+OTR scaffolds showed more compressed pores than Col I, but pore morphology was similar in both untreated (noncrosslinked) scaffolds (Figure 1A and Supporting Information Figure S3). For in vitro and in vivo studies, scaffolds were sterilized by gamma radiation. Then, the amount of free amine groups was used to calculate the crosslinking degree (i.e., \sim 62%), which did not change after sterilization (Figure 1B). The amount

of bound OTR4120 to collagen scaffolds remained constant with $24\pm5\,\mu g$ OTR4120/mg collagen scaffold in crosslinked scaffolds before and after sterilization, showing that gamma sterilization did not affect the amount of OTR4120 bound to scaffolds after crosslinking. However, the OTR4120 amount slightly increased in untreated Col I+OTR after sterilization (Figure 1B).

3.2 | Presence of OTR4120 and SHH in Collagen-Based Scaffolds

OTR4120 is a heparan sulphate mimetic capable of binding heparin-binding sites of proteins such as effector molecules and, to a lesser extent, collagen. SHH has positively charged amino acid residues that interact with OTR4120. Col I and Col I+OTR scaffolds captured similar amounts of SHH, as quantified by Western blotting (Figure 2A,B). Col I contained $0.15 \pm 0.10 \,\mu g$ SHH/mg scaffold and Col I+OTR captured $0.13 \pm 0.20 \,\mu\text{g/mg}$. After consecutive washes, the SHH was not detected in the wash solutions (Supporting Information Figure S4). The distribution of OTR4120 and SHH in the scaffolds was visualized using immunofluorescence assays. The antibody for heparan sulphate cross-reacts with OTR4120. Staining for heparan sulphate showed an even localization of OTR4120 in the whole scaffold of Col I+OTR, while there was no staining in the Col I scaffold. SHH bound to both types of scaffolds but was concentrated at the edge of Col I scaffolds. SHH penetrated deeper inside the Col I+OTR scaffold, showing some overlap in the merged image of OTR4120 and SHH (Figure 2C).

3.3 | In Vitro Analysis With Human Macrophages

Since incorporation of OTR4120 and SHH in collagen scaffolds may affect the macrophage phenotype, we seeded M0

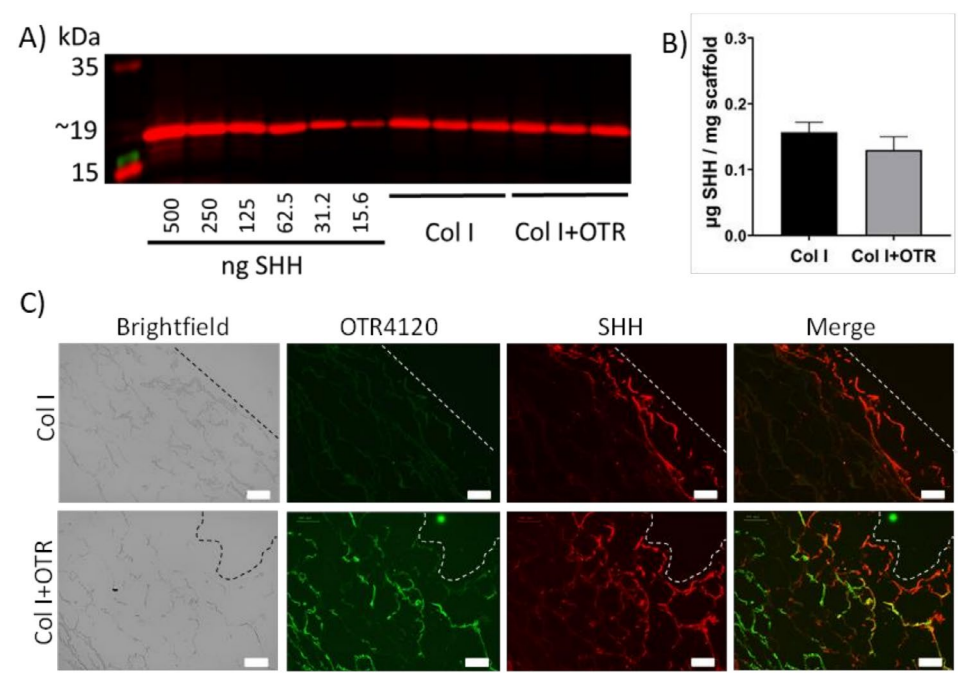


FIGURE 2 | SHH bound to Col I and Col I + OTR scaffolds after incubation with $3.5 \mu g$ SHH/ml overnight. (A) SHH detection using western blotting. Positive bands are stained in red around $19 \, k$ Da. The image shows the calibration curve, Col I and Col I + OTR scaffolds from three different batches. (B) Quantification of SHH bound to scaffolds from bands on Western blots (n = 3) gave no significant differences. (C) Detection of OTR4120 (green) and SHH (red) using immunostaining. OTR4120 was identified with single chain antibody HS4C3 against heparan sulphate. SHH was concentrated at the edge of the Col I scaffold while it showed a deeper penetration in OTR-containing scaffolds. Dashed line indicates the outer edge of the scaffold. Scale bar is $100 \, \mu m$.

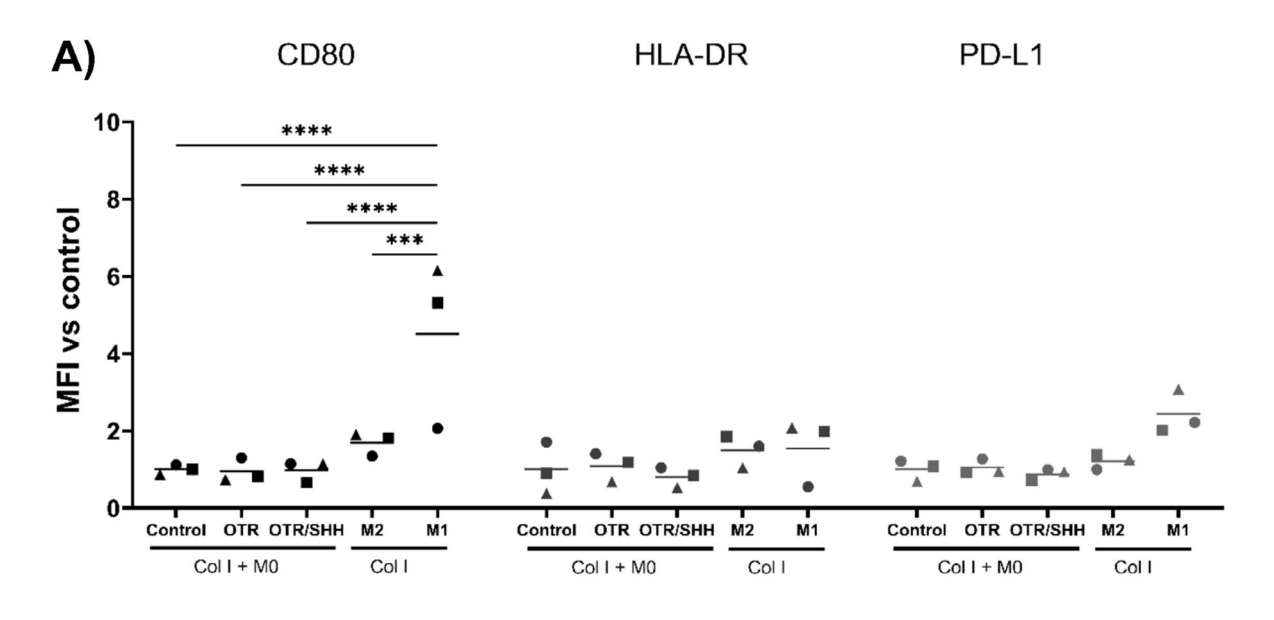
macrophages to evaluate whether scaffold components would convert the cells toward an M1 (pro-inflammatory) or M2 (pro-healing) subtype. Flow cytometry was used to measure the cell surface markers. Additional controls included M1-like and M2-like macrophages, which were seeded on Col I scaffolds to analyse the cell surface markers on non-functionalized scaffolds.

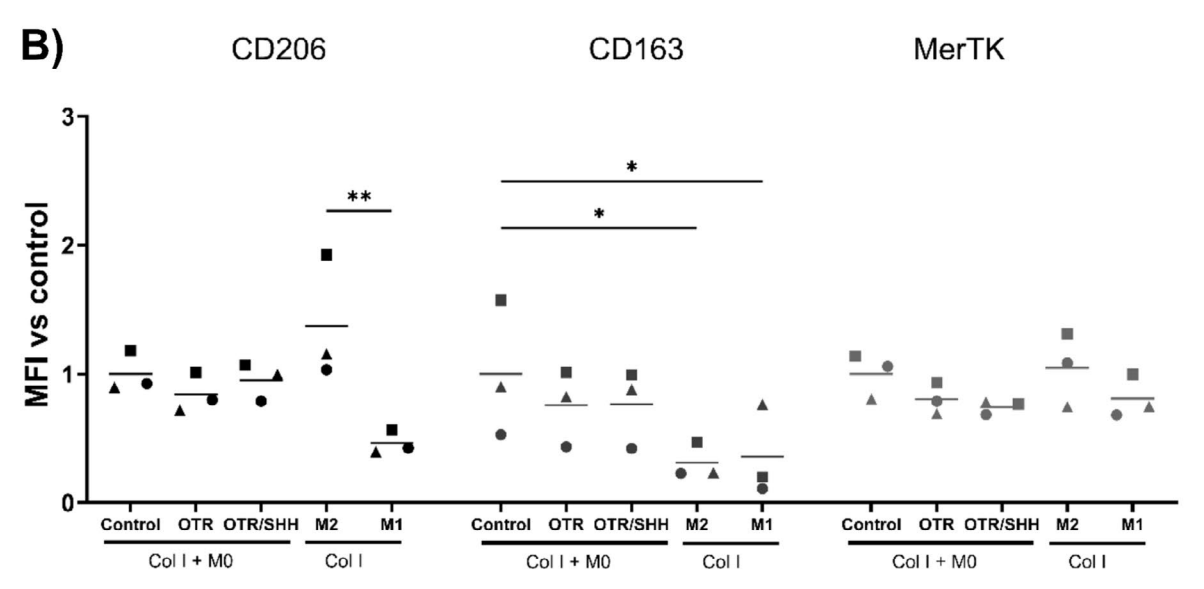
OTR4120 and SHH appeared to modulate macrophage polarization by slightly reducing certain pro-inflammatory markers and modestly enhancing anti-inflammatory cytokine production. The three conditions, Col I, Col I+OTR and Col I + OTR/SHH, tended to show lower expression of CD markers associated with pro-inflammatory phenotypes, such as CD80, HLA-DR and PD-L1 (Figure 3A), than the M1-like macrophages control. In contrast, M2-associated markers showed no significant differences across scaffold conditions seeded with M0 macrophages (Figure 3B), although CD163 expression was significantly higher in control and slightly elevated in OTR (p = 0.26) and SHH (p = 0.25) compared to the M2-like control. Cytokine analysis of culture supernatants (Figure 3G-I) revealed reduced IL12 levels in all M0-seeded scaffold conditions—Col I (p = 0.11), OTR (p = 0.10) and SHH (p = 0.08)—relative to M1-like macrophages. IL10 was significantly higher (~30-fold) in the Col I+OTR condition compared to all conditions, while the 10-fold increase in OTR/ SHH was not statistically significant (p = 0.22). These findings suggest a trend toward an anti-inflammatory profile, particularly with OTR treatment, though variability between donors limits definitive conclusions.

3.4 | OTR4120 In Col I Scaffolds Enhance Wound Healing

Col I and Col I + OTR scaffolds were implanted in full-thickness wounds in rats. To compare the wound healing efficiency, untreated wounds were used as controls for scaffold treatment, while Col I was used as a control to assess the effect of incorporation of OTR4120. After surgery, rats experienced weight loss and discomfort from bandaging. To improve well-being, adjustments were made, including substituting the elastic band (Petflex) for a softer cotton material (2,310,057, Kruidvat, NL). Despite these efforts, two rats died during the third postoperative week—one was found dead in its cage, likely due to bandage-related distress, and another was euthanized at a humane endpoint following marked weight loss and signs of discomfort. The remaining seven animals completed the 28-day study period.

Macroscopic photos of the wound area were taken at day 0, 7, 14, 21 and 28, but accurate wound measurements could not be performed after day 14 due to scab formation (Figure 4A). To avoid disrupting the underlying neo-epidermis and granulation tissue, scabs were left intact, as they typically detached only after 5 weeks in this full-thickness wound model, consistent with previous observations in a similar study with porous collagen biomaterials that followed healing up to 56 days [34]. On day 14, wounds treated with scaffolds presented less wound contraction at day 7 with 17% in Col I and Col I+OTR compared to 40% in the untreated group. This difference increased by day 14, where the untreated wounds had contracted more than 78% in contrast to the treated scaffolds, with 24% and 26% for Col I and





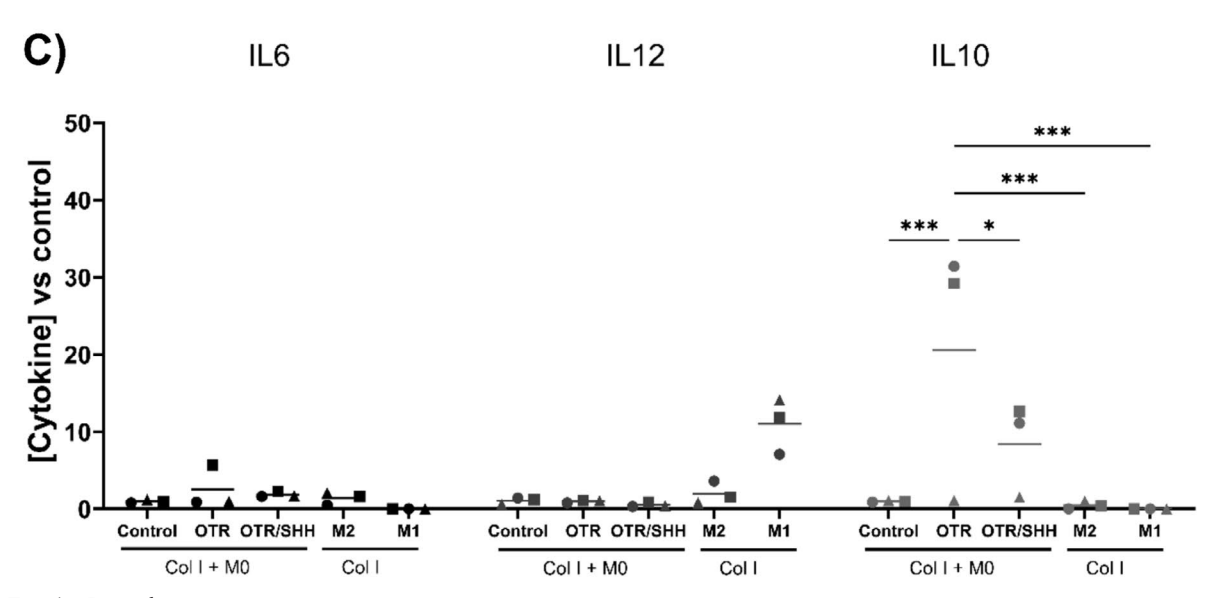


FIGURE 3 | Legend on next page.

FIGURE 3 | Effect of OTR4120 and/or SHH in collagen scaffolds on primary human macrophages. Type I collagen scaffolds with M0 macrophages were used as control. As secondary controls, Col I with either M1 or M2 macrophages were included. Mean fluorescence intensity (MFI) was measured by flow cytometry for (A) M1 associated markers and (B) M2 associated markers. (C) Cytokine concentrations in the supernatants. Every donor is represented with a different symbol. Data are represented as mean \pm SD (n = 3). p < 0.05, **p < 0.01, ***p < 0.001 and ****p < 0.0001.

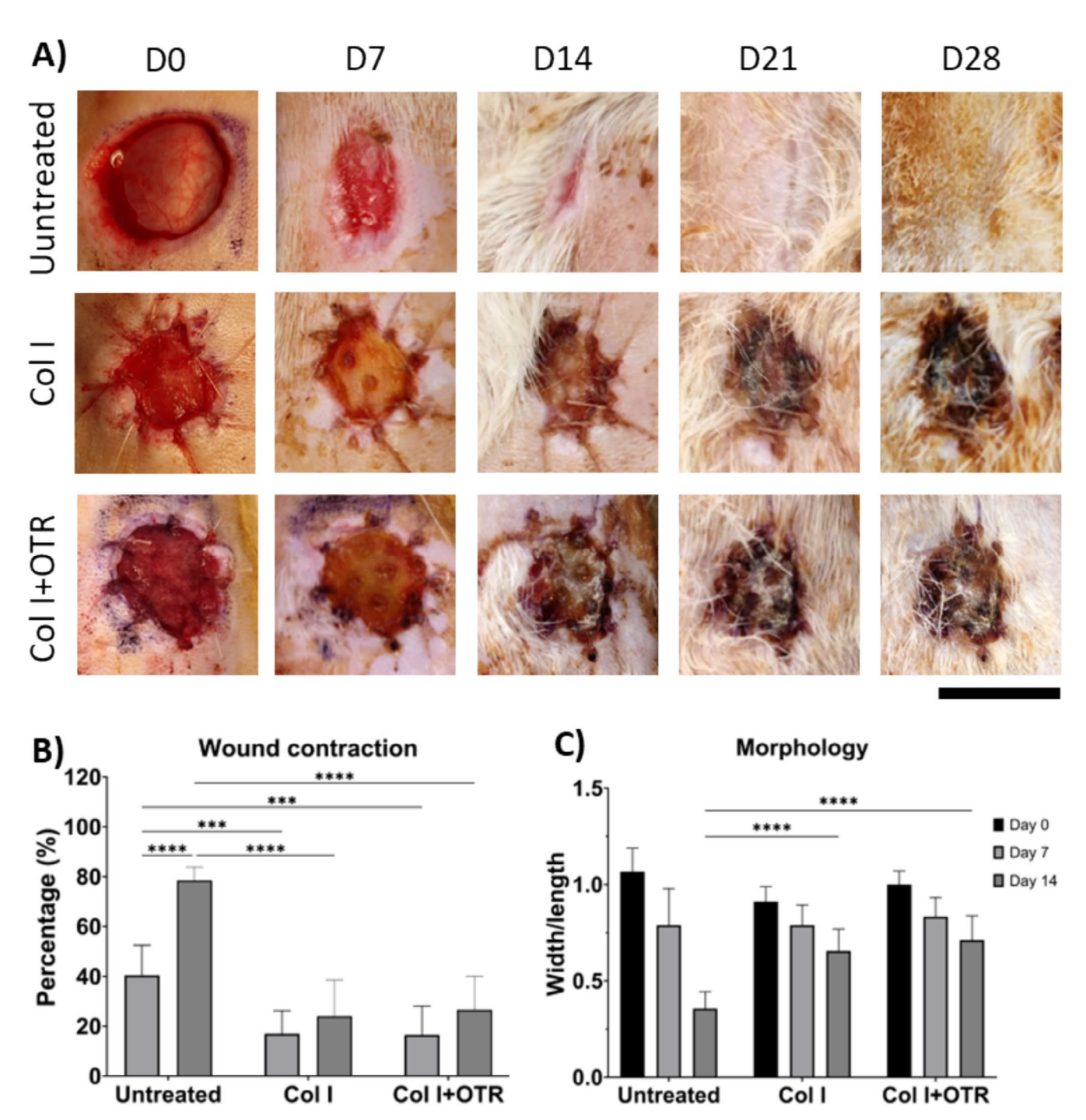


FIGURE 4 | Wound contraction and morphology assessment in rats. Twelve millimetre wounds were created on the back of the rats and left untreated or treated with Col I or Col I + OTR scaffolds. (A) Representative macroscopical images of the wounds, from day 0 to day 28. Scale bar is 1 cm. (B) Wound contraction at day 7 and day 14 compared to day 0. (C) Wound morphology assessment using the width to length ratio of the wound., where 1 represents a symmetric circular shape. Note that circular patterns visible in Col I and Col I + OTR groups result from the texture of the wound dressing. These superficial imprints persist in the scabs due to drying but did not interfere with the underlying healing process. Values are represented as the mean \pm SD (n=9). Comparison between groups was analysed using 2-way ANOVA. **p<0.01, ***p<0.001, ***p<0.0001.

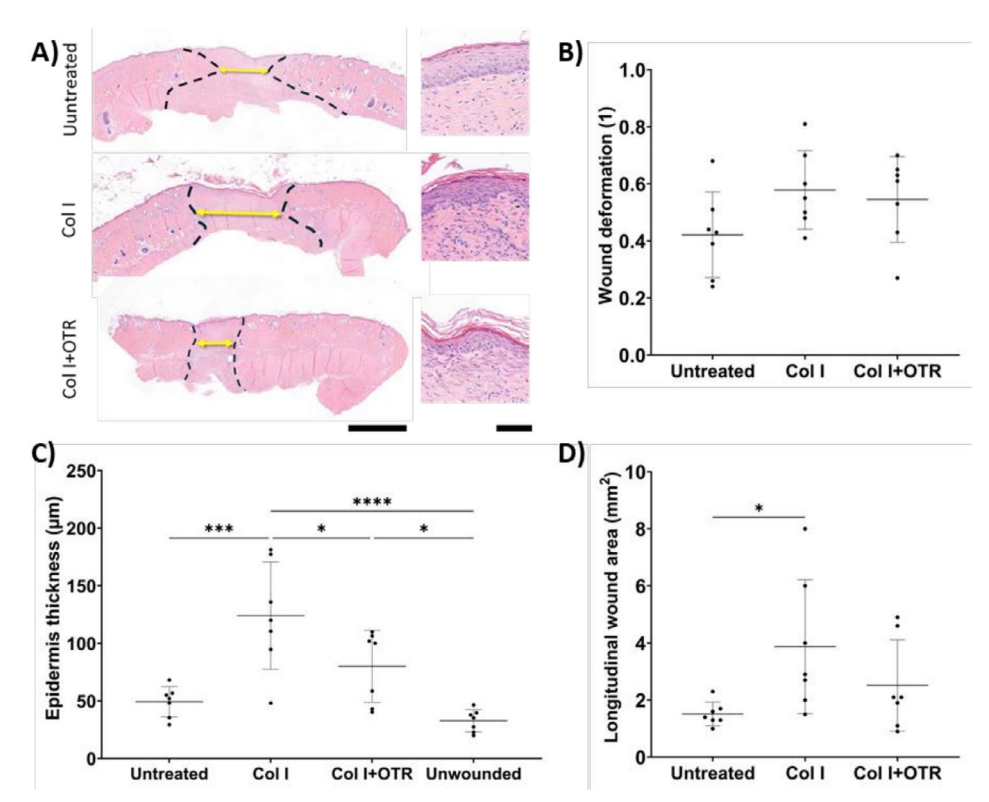


FIGURE 5 | Histological analysis of wound areas on day 28. (A) H&E staining of representative tissue sections. The dotted line is the interface between granulation tissue and unwounded skin, whereas the yellow arrow indicates the middle width of the dermis in the wound. Left images depict the complete tissue sample, while images on the right are an enlargement of the epidermal layer on the wound. Scale bar for skin overview is 2 mm and for epidermis $60 \,\mu\text{m}$. (B) Microscopical wound deformation calculated as a comparison between the length of the wound between the middle and top of the dermis. Values closer to 0 represent a higher deformation. (C) Epidermal thickness above the granulation tissue. (D) Wound area in the longitudinal plane visible by granulation tissue and delimited by dotted lines on histology. Data represent mean \pm SD (n = 7). One-way ANOVA with Tukey's multiple comparison test was used for statistical analysis. *p < 0.005, ****p < 0.0001.

Col I+OTR, respectively (Figure 4B). These trends suggest that scaffold-treated wounds exhibit more gradual contraction. The morphology of wounds during closing may impact the development of scars. The full-thickness wounds created on the back of the rats were a round circle of 12 mm diameter at day 0 with a width/length of \sim 1. On day 14, the untreated wounds tended to become oval shaped with a width/length ratio close to 0.36 in comparison to 0.65 in Col I and 0.71 in Col I+OTR (Figure 4C).

The full wound areas with surrounding healthy skin were taken at day 28 and analysed using (immuno) histochemistry. H&E staining of cross-sections of day 28 reflected our macroscopic observations of a significant contraction from untreated condition followed by collagen scaffolds with and without OTR4120. Granulation tissue formed an hourglass shape, which was most pronounced in untreated wounds as observed with the dotted line, indicating a higher wound deformation compared to scaffold conditions (Figure 5A,B). The epidermis was significantly thicker in Col I followed by Col I+OTR with untreated condition featuring a similar thickness to unwounded skin (Figure 5C). The wound area was larger in Col I condition compared to untreated wounds, probably due to the reduced skin contraction (Figure 5D).

To evaluate the degradation of scaffolds, residual collagen material was scored. Collagen scaffold remnants can be easily differentiated from native collagen due to their thicker collagen bundles and intense blue staining using Masson's trichrome blue (Figure 6A).

By day 28, there were still some remnants in Col I condition, followed by OTR4120-containing scaffolds but with a mean score of less than 1. We semi-quantitatively scored myofibroblasts, macrophages and blood vessels within the granulation tissue to evaluate whether the different conditions influenced cell recruitment and/or proliferation. No significant differences were found in the number of myofibroblasts (Figure 6B). An overview with α -SMA staining showed that myofibroblasts had migrated to the wound area from the bottom and the wound edges (Supporting Information Figure S5). Treatment with OTR-containing scaffolds was associated with an increased number of macrophages (Figure 6C). Scaffold treatments also appeared to increase angiogenesis compared to the untreated wounds (Figure 6D).

Appendages such as hair follicles and sebaceous glands appeared next to the wound margins (approximately $300\,\mu m$ away from the margin) (Figure 7A). The density of hair follicles per area remained similar in all conditions (Figure 7B). In contrast, Col I+OTR slightly increased the content of sebaceous glands at the wound edge compared to untreated wounds (Figure 7C).

4 | Discussion

Scarring remains a significant clinical challenge, often leading to morbidity and impaired skin regeneration. Therefore, there is

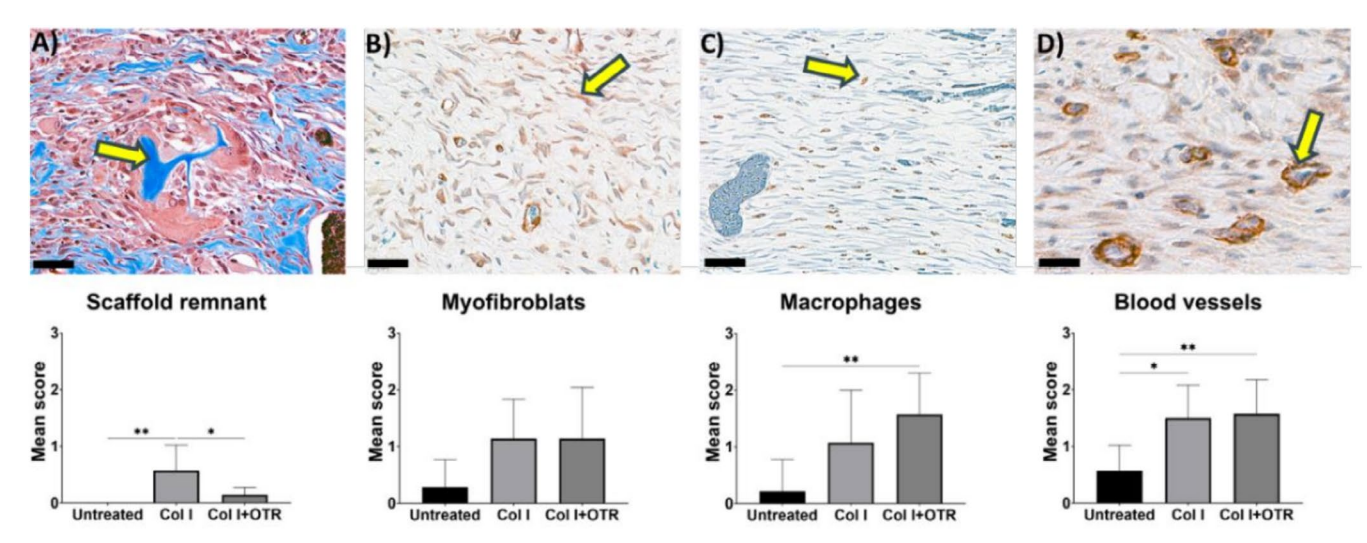


FIGURE 6 | Histological analysis of day 28 tissue samples of various treatments. The top row shows histological examples, and the bottom row presents the semi-quantitative scoring. (A) Remaining collagen scaffold visualized using trichrome blue. OTR-containing scaffold showed more degradation. (B) Myofibroblasts stained for alpha smooth muscle actin (α -SMA) visualized as elongated cells with blue nuclei. (C) Macrophages stained with CD68 marker, Col I+OTR showed higher numbers. (D) Blood vessels were identified using α -SMA staining for mature blood vessels. More angiogenesis was seen for scaffold-treated wounds. Arrows depict examples of the corresponding parameter. Sections were scored for these aspects from 0 (not present) to 3 (abundant). Data are represented as mean \pm SD (n=7). Scale bars are 40 μ m. *p<0.05, **p<0.01.

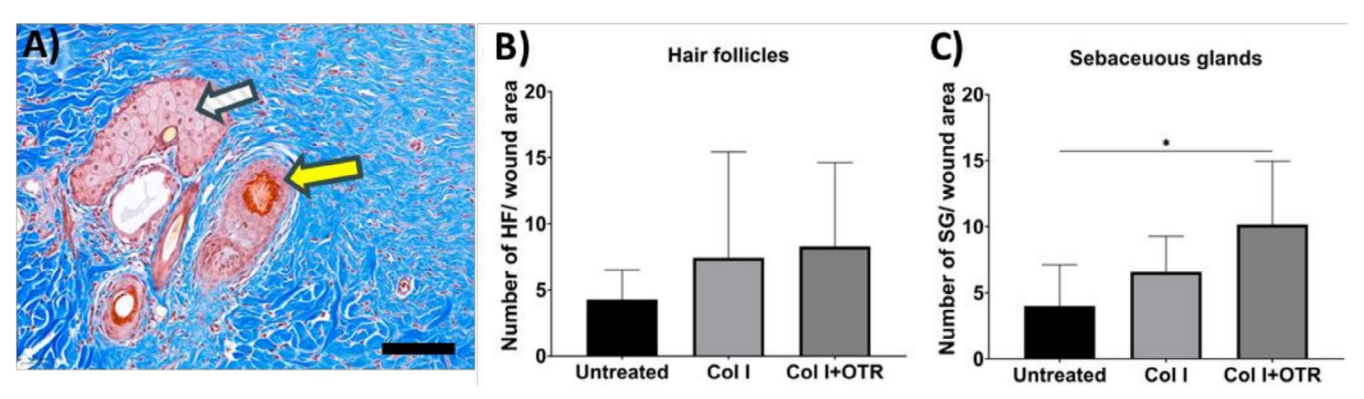


FIGURE 7 | Quantitative histological analysis of appendages in healed skin. (A) Representative histological image showing hair follicles (HF, yellow arrow) and sebaceous glands (SG, grey arrow) in the transitional wound area visualized with Masson's trichrome blue staining. (B, C) Quantification of hair follicles (B) and sebaceous glands (C) in the adjacent wound area ($<300 \,\mu\text{m}$). Scale bar is $100 \,\mu\text{m}$. *p < 0.05, **p < 0.01.

a pressing need for advanced biomaterials capable of promoting effective skin healing. In this study, we created innovative collagen scaffolds containing RGTA OTR4120, a heparan sulphate mimetic molecule proven to improve wound healing in liquid format, such as CACIPLIQ20 [35].

In order to use skin substitutes in vivo, scaffolds were chemically crosslinked and sterilized by gamma irradiation. This sterilization step did not affect the crosslinking degree nor the amount of OTR4120 retained on crosslinked scaffolds, as OTR4120 was already covalently bound prior to sterilization. Interestingly, untreated (non-crosslinked) Col I + OTR scaffolds showed a slightly higher signal for OTR4120 after sterilization compared to their non-sterilized counterparts. Gamma rays can induce free radical formation and chemical modifications even in freeze-dried scaffolds, including chain scission or formation of new covalent bonds through oxidative pathways [36–38]. These alterations may facilitate more efficient papain digestion

by breaking collagen chains and increasing the release of embedded OTR4120. In contrast, chemically crosslinked scaffolds are more resistant to such changes, and the amount of retained OTR4120 remained consistent before and after sterilization.

We also tested the capability of OTR4120 to bind the effector molecule SHH, which is a promising effector molecule for skin regeneration. It is upregulated during embryonic development, promoting nerve growth [39], epidermal development [23] and hair follicle morphogenesis [40]. OTR4120 has been reported to bind heparin-binding growth factors such as FGF, VEGF and TGF β [21]. In our study, collagen scaffolds with and without OTR4120 bound similar amounts of the heparin-binding growth factor SHH (0.13–0.15 μg SHH/mg scaffold). Similarly, another study on Col I + OTR showed a similar amount of FGF-2 binding compared to Col I but revealed a more gradual release of FGF2 in OTR-containing scaffolds [28]. A slower release of SHH may benefit later stages of wound healing, such as re-epithelization

and stimulation of hair follicle neogenesis. Immunostainings showed that SHH penetrated deeper in Col I+OTR scaffolds, while concentrating at the edges in Col I. A previous study using collagen-heparin scaffolds incubated with $10\,\mu\text{g/mL}$ SHH (nearly three times our $3.5\,\mu\text{g/mL}$) also found SHH primarily at the edges [25].

To assess the effect of OTR4120 and SHH on immune cells. in vitro testing was performed by culturing M0 macrophages on collagen scaffolds. Overall, it seems that collagen scaffolds seeded with M0 macrophages promote a macrophage phenotype more akin to M2-like than M1-like phenotypes. Although not statistically significant, Col I+OTR/SHH treatment consistently showed lower mean expression of M1-associated markers, indicating a trend toward reduced pro-inflammatory macrophage activation. This aligns with previous reports where SHH reduced M1-related markers in macrophage cultures [41]. The largest effect of OTR4120 was observed in the expression of IL10, being nearly 30 times higher in two donors compared to Col I. IL10 is mainly produced by the M2clike phenotype [42] and can reduce inflammation, inhibit the transformation of fibroblasts into myofibroblasts and increase collagen reorganization [43-45], resulting in skin repair with less scarring.

To study the effect of OTR4120 in acute deep wounds, collagen scaffolds with incorporated OTR4120 were applied on full-thickness wounds in a rat model over 28 days. By day 14, scaffold-treated wounds showed less macroscopic contraction compared to untreated wounds. A rapid contraction often leads to fibrosis and scar formation, a hallmark of mammalian healing but less pronounced in rodents [46]. In contrast, species capable of scarless regeneration, such as axolotls, exhibit delayed contraction and ECM deposition [47]. While we did not assess biomechanical properties of the scaffolds in this study, similar crosslinked type I collagen scaffolds had a Young's modulus of approximately 0.4 kPa [48], which is considerably lower than the ~5 kPa threshold reported to induce fibroblast-to-myofibroblast transition [49], suggesting that our scaffolds are relatively soft and unlikely to mechanically restrain the wound or hold it open. In addition, Col I+OTR scaffolds helped preserve a more rounded wound shape, which may suggest a more uniform healing that could lead to less scar formation [50]. Although round wounds were initially created to evenly distribute mechanical forces, untreated wounds contracted faster and formed an oval shape. Histological analysis revealed that untreated wounds, despite faster macroscopic contraction, exhibited greater deformation, indicating less coordinated healing and a higher risk of contractures. In contrast, scaffold-treated wounds showed slower, more organized closure with reduced deformation, supporting a more controlled healing process and potentially minimizing scarring [51, 52]. Re-epithelialization was complete across all conditions, but OTR-treated wounds showed a trend toward an epidermal thickness closer to native skin and with a slightly smaller wound area in the longitudinal section than Col I alone, which may be the result of a less rigid skin [53] and improved wound healing.

Immunostaining revealed that scaffolds delayed ECM deposition, with more presence of granular tissue and slightly elevated levels of myofibroblasts and macrophages than in

untreated wounds. Porous scaffolds facilitated cell infiltration from wound edges and deeper layers. Particularly, OTRtreated wounds displayed a higher macrophage presence as evidenced by CD68 staining, which might be related to the faster scaffold degradation (Figure 6A,B). In contrast, a previous study in a foetal sheep model using collagen-heparin scaffolds with growth factors found more residual scaffold and lower macrophage presence (scoring < 1, scale 0-3) [17]. This suggests that OTR4120 influences macrophage recruitment in adult rats, leading to accelerated scaffold degradation. A higher number of blood vessels was seen in scaffold-treated wounds, aligning with the proliferative phase [54]. While OTR4120 did not affect hair follicle abundance, it increased the number of sebaceous glands in the adjacent wound area. Given OTR4120's ability to bind heparin-binding effector molecules [55], it may interact with local growth factors, such as WNT, SHH, BMP and FGF [56], which are involved in sebaceous gland development [57].

A limitation of this study is that the Col I+OTR/SHH scaffold and OTR4120 alone were not evaluated in vivo. In vitro studies with SHH were limited to macrophages, thereby missing potential interactions with other relevant cells such as dermal papilla cells, neurons and epidermal cells. Future research should explore these interactions to better understand SHH's broader potential in skin regeneration. Additionally, the animal model presents limitations, as rats possess a panniculus carnosus layer which produces rapid wound contraction, which is absent in human skin [58]. Unlike general practice in humans and larger animal studies, we did not apply split-thickness skin grafts in these rodents, as this is highly challenging, limiting the ability to fully replicate skin treatments in humans. Pigs, with ECM skin more similar to human skin and comparable healing times, could be considered as an alternative animal model for future preclinical studies [46].

In conclusion, we successfully constructed chemically cross-linked porous collagen scaffolds with bound RGTA OTR4120, which remained stable after gamma sterilization. These scaffolds retained the ability to bind the effector molecule SHH and showed a trend toward a pro-healing M2-like macrophage phenotype in culture. In a rat full-thickness wound model, collagen-OTR scaffolds modestly influenced wound healing dynamics by supporting ECM remodelling, maintaining improved wound morphology and moderating epidermal thickness, which may contribute to reducing fibrosis and improving skin regeneration outcomes. This study provides preliminary evidence that OTR4120 could be a promising addition to acellular skin substitutes for improving acute wound healing.

Acknowledgements

The authors thank the Radboud Technology Center Microscopy for the use of the Scanning Electron Microscope and Elly Versteeg for the development and optimization of the used dot blot method. We appreciate the help from Steven Teerenstra with the power analysis for rat experiments as well as Hans Smola (Hartmann AG) for clinical advice about wound dressings for the rat experiments. We thank Maikel School, Tim Peters and the animal research facility staff for their support with the rat experiments.

Conflicts of Interest

A.C. and F.C. are current employees of OTR3, and D.B. is CEO of OTR3. However, the views presented in this research article remain independent and were not influenced by the company.

Data Availability Statement

The data that support the findings of this study are available in the Supporting Information of this article.

References

- 1. T. J. Schaefer and O. Nunez Lopez, "Burn Resuscitation and Management," in *StatPearls* (StatPearls Publishing Copyright 2025, StatPearls Publishing LLC, 2023).
- 2. M. Takeo, W. Lee, and M. Ito, "Wound Healing and Skin Regeneration," *Cold Spring Harbor Perspectives in Medicine* 5, no. 1 (2015): a023267, https://doi.org/10.1101/cshperspect.a023267.
- 3. L. C. Cancio, D. J. Barillo, R. D. Kearns, et al., "Guidelines for Burn Care Under Austere Conditions: Surgical and Nonsurgical Wound Management," *Journal of Burn Care & Research* 38, no. 4 (2017): 203–214, https://doi.org/10.1097/bcr.0000000000000368.
- 4. A. S. García-Salinas, G. A. Mecott, M. García-Pérez, et al., "Decreased Pain in Split-Thickness Skin Graft Donor Sites With the Use of a Non-Adherent Polyurethane Dressing," *Medicina Universitaria* 17, no. 69 (2015): 196–202, https://doi.org/10.1016/j.rmu.2015.07.001.
- 5. M. C. T. Bloemen, M. C. E. van, van Leeuwen, N. E. van Vucht, P. P. M. Zuijlen, and E. Middelkoop, "Dermal Substitution in Acute Burns and Reconstructive Surgery: A 12-Year Follow-Up," *Plastic and Reconstructive Surgery* 125, no. 5 (2010): 1450–1459, https://doi.org/10.1097/PRS.0b013e3181d62b08.
- 6. A. S. van den Bosch, R. A. F. Verwilligen, A. Pijpe, et al., "Outcomes of Dermal Substitutes in Burns and Burn Scar Reconstruction: A Systematic Review and Meta-Analysis," *Wound Repair and Regeneration* 32, no. 6 (2024): 960–978, https://doi.org/10.1111/wrr.13226.
- 7. S. M. Karppinen, R. Heljasvaara, D. Gullberg, K. Tasanen, and T. Pihlajaniemi, "Toward Understanding Scarless Skin Wound Healing and Pathological Scarring," *F1000Research* 8 (2019), https://doi.org/10.12688/f1000research.18293.1.
- 8. A. Zaidi and L. Green, "Physiology of Haemostasis," *Anaesthesia & Intensive Care Medicine* 23, no. 2 (2022): 111–117, https://doi.org/10.1016/j.mpaic.2021.10.023.
- 9. Y. Su, J. Gao, P. Kaur, and Z. Wang, "Neutrophils and Macrophages as Targets for Development of Nanotherapeutics in Inflammatory Diseases," *Pharmaceutics* 12, no. 12 (2020): 1222, https://doi.org/10.3390/pharmaceutics12121222.
- 10. M. T. Silva, "Macrophage Phagocytosis of Neutrophils at Inflammatory/Infectious Foci: A Cooperative Mechanism in the Control of Infection and Infectious Inflammation," *Journal of Leukocyte Biology* 89, no. 5 (2011): 675–683, https://doi.org/10.1189/jlb.0910536.
- 11. H. Zheng, X. Cheng, L. Jin, S. Shan, J. Yang, and J. Zhou, "Recent Advances in Strategies to Target the Behavior of Macrophages in Wound Healing," *Biomedicine & Pharmacotherapy* 165 (2023): 115199, https://doi.org/10.1016/j.biopha.2023.115199.
- 12. M. Alhajj and A. Goyal, *Physiology, Granulation Tissue StatPearls* (StatPearls Publishing, 2022).
- 13. I. V. Yannas and D. S. Tzeranis, "Mammals Fail to Regenerate Organs When Wound Contraction Drives Scar Formation," *npj Regenerative Medicine* 6, no. 1 (2021): 39, https://doi.org/10.1038/s41536-021-00149-9.
- 14. M. Piipponen, D. Li, and N. X. Landén, "The Immune Functions of Keratinocytes in Skin Wound Healing," *International Journal of*

- *Molecular Sciences* 21, no. 22 (2020): 8790, https://doi.org/10.3390/ijms2 1228790.
- 15. B. Li and J. H. Wang, "Fibroblasts and Myofibroblasts in Wound Healing: Force Generation and Measurement," *Journal of Tissue Viability* 20, no. 4 (2011): 108–120, https://doi.org/10.1016/j.jtv.2009. 11.004.
- 16. S. T. M. Nillesen, G. Lammers, R. G. Wismans, et al., "Design and in Vivo Evaluation of a Molecularly Defined Acellular Skin Construct: Reduction of Early Contraction and Increase in Early Blood Vessel Formation," *Acta Biomaterialia* 7, no. 3 (2011): 1063–1071, https://doi.org/10.1016/j.actbio.2010.10.011.
- 17. C. Oostendorp, P. J. Geutjes, F. Smit, et al., "Sustained Postnatal Skin Regeneration Upon Prenatal Application of Functionalized Collagen Scaffolds," *Tissue Engineering, Part A* 27, no. 1–2 (2021): 10–25, https://doi.org/10.1089/ten.tea.2019.0234.
- 18. K. J. Bame, "Heparanases: Endoglycosidases That Degrade Heparan Sulfate Proteoglycans," *Glycobiology* 11, no. 6 (2001): 91R–98R, https://doi.org/10.1093/glycob/11.6.91R.
- 19. J. Neck, B. Tuk, D. Barritault, and M. Tong, "Heparan Sulfate Proteoglycan Mimetics Promote Tissue Regeneration: An Overview," in *Tissue Regeneration From Basic Biology to Clinical Application* (InTech Open, 2012), 69–92.
- 20. Y. Ikeda, S. Charef, M.-O. Ouidja, et al., "Synthesis and Biological Activities of a Library of Glycosaminoglycans Mimetic Oligosaccharides," *Biomaterials* 32, no. 3 (2011): 769–776, https://doi.org/10.1016/j.biomaterials.2010.09.043.
- 21. D. Barritault, M. Gilbert-Sirieix, K. L. Rice, et al., "RGTA or ReGeneraTing Agents Mimic Heparan Sulfate in Regenerative Medicine: From Concept to Curing Patients," *Glycoconjugate Journal* 34, no. 3 (2017): 325–338, https://doi.org/10.1007/s10719-016-9744-5.
- 22. N. N. Potekaev, O. B. Borzykh, G. V. Medvedev, et al., "The Role of Extracellular Matrix in Skin Wound Healing," *Journal of Clinical Medicine* 10, no. 24 (2021): 5947, https://doi.org/10.3390/jcm10245947.
- 23. Y. Abe and N. Tanaka, "Roles of the Hedgehog Signaling Pathway in Epidermal and Hair Follicle Development, Homeostasis, and Cancer," *Journal of Developmental Biology* 5, no. 4 (2017): 12, https://doi.org/10.3390/jdb5040012.
- 24. K. Takaya, N. Aramaki-Hattori, S. Sakai, K. Okabe, and K. Kishi, "Effect of Sonic Hedgehog on the Regeneration of Epidermal Texture Patterns," *Biomedicine* 10, no. 12 (2022): 3099, https://doi.org/10.3390/biomedicines10123099.
- 25. P. J. E. Uijtdewilligen, E. M. M. Versteeg, C. Gilissen, et al., "Towards Embryonic-Like Scaffolds for Skin Tissue Engineering: Identification of Effector Molecules and Construction of Scaffolds," *Journal of Tissue Engineering and Regenerative Medicine* 10, no. 1 (2016): E34–E44, https://doi.org/10.1002/term.1725.
- 26. D. M. Whalen, T. Malinauskas, R. J. Gilbert, and C. Siebold, "Structural Insights Into Proteoglycan-Shaped Hedgehog Signaling," *Proceedings of the National Academy of Sciences of the United States of America* 110, no. 41 (2013): 16420–16425, https://doi.org/10.1073/pnas.13100 97110.
- 27. J. Chakrabarti, M. Dua-Awereh, M. Schumacher, et al., "Sonic Hedgehog Acts as a Macrophage Chemoattractant During Regeneration of the Gastric Epithelium," *npj Regenerative Medicine* 7, no. 1 (2022): 3, https://doi.org/10.1038/s41536-021-00196-2.
- 28. M. Gansevoort, S. Wentholt, G. Li Vecchi, et al., "Next-Generation Biomaterials for Wound Healing: Development and Evaluation of Collagen Scaffolds Functionalized With a Heparan Sulfate Mimic and Fibroblast Growth Factor 2," *Journal of Functional Biomaterials* 16, no. 2 (2025): 51, https://doi.org/10.3390/jfb16020051.
- 29. J. S. Pieper, A. Oosterhof, P. J. Dijkstra, J. H. Veerkamp, and T. H. van Kuppevelt, "Preparation and Characterization of Porous Crosslinked

- Collagenous Matrices Containing Bioavailable Chondroitin Sulphate," *Biomaterials* 20, no. 9 (1999): 847–858, https://doi.org/10.1016/s0142-9612(98)00240-3.
- 30. D. Papy-Garcia, V. Barbier-Chassefière, V. Rouet, et al., "Nondegradative Sulfation of Polysaccharides. Synthesis and Structure Characterization of Biologically Active Heparan Sulfate Mimetics," *Macromolecules* 38, no. 11 (2005): 4647–4654, https://doi.org/10.1021/ma048485p.
- 31. J. Elias, B. A. Matheson, and L. Gower, "Influence of Crosslinking Methods on Biomimetically Mineralized Collagen Matrices for Bone-Like Biomaterials," *Polymers (Basel)* 15, no. 9 (2023): 1981, https://doi.org/10.3390/polym15091981.
- 32. T. M. Clausen, G. Kumar, E. K. Ibsen, et al., "A Simple Method for Detecting Oncofetal Chondroitin Sulfate Glycosaminoglycans in Bladder Cancer Urine. Cell Death," *Discovery* 6, no. 1 (2020): 65, https://doi.org/10.1038/s41420-020-00304-z.
- 33. L. A. A. Damen, E. M. A. van de Westerlo, E. M. M. Versteeg, T. van Wessel, W. F. Daamen, and T. H. van Kuppevelt, "Construction and Evaluation of an Antibody Phage Display Library Targeting Heparan Sulfate," *Glycoconjugate Journal* 37, no. 4 (2020): 445–455, https://doi.org/10.1007/s10719-020-09925-z.
- 34. R. Krymchenko, N. Avila-Martinez, M. Gansevoort, et al., "Collagen-Elastin Dermal Scaffolds Enhance Tissue Regeneration and Reduce Scarring in Preclinical Models," *Materials Today Bio* 34 (2025): 102239, https://doi.org/10.1016/j.mtbio.2025.102239.
- 35. D. Barritault, "Overview of 10 Years of Practice With CACIPLIQ20 Matrix Therapy as a Healing Agent for Hard to Heal Wounds: Efficacy, Cost-Effectiveness and Future Perspectives," *Wound Medicine* 28 (2020): 100180, https://doi.org/10.1016/j.wndm.2020.100180.
- 36. J. M. Patel, R. C. Jackson, G. L. Schneider, S. A. Ghodbane, and M. G. Dunn, "Carbodiimide Cross-Linking Counteracts the Detrimental Effects of Gamma Irradiation on the Physical Properties of Collagen-Hyaluronan Sponges," *Journal of Materials Science. Materials in Medicine* 29, no. 6 (2018): 75, https://doi.org/10.1007/s10856-018-6056-2.
- 37. D. B. Crocker, T. M. Hering, O. Akkus, M. E. Oest, and C. M. Rimnac, "Dose-Dependent Effects of Gamma Radiation Sterilization on the Collagen Matrix of Human Cortical Bone Allograft and Its Influence on Fatigue Crack Propagation Resistance," *Cell and Tissue Banking* 25, no. 3 (2024): 735–745, https://doi.org/10.1007/s10561-024-10135-2.
- 38. S. M. Jeong, H. H. Kim, S. H. Ryu, et al., "Effects of Gamma Irradiation on Inhibition of Urease Activity and Fishy Smell in Mackerel (*Scomber Japonicus*) During Refrigerated Storage," *Journal of Microbiology and Biotechnology* 32, no. 6 (2022): 808–815, https://doi.org/10.4014/jmb.2112.12037.
- 39. Y. H. Belgacem, A. M. Hamilton, S. Shim, K. A. Spencer, and L. N. Borodinsky, "The Many Hats of Sonic Hedgehog Signaling in Nervous System Development and Disease," *Journal of Developmental Biology* 4, no. 4 (2016): 35.
- 40. X. Sun, A. Are, K. Annusver, et al., "Coordinated Hedgehog Signaling Induces New Hair Follicles in Adult Skin," *eLife* 9 (2020): e46756, https://doi.org/10.7554/eLife.46756.
- 41. J. Zhang, Z. He, C. Xiong, et al., "SHH Induces Macrophage Oxidative Phosphorylation and Efferocytosis to Promote Scar Formation," *Cell Communication and Signaling* 22, no. 1 (2024): 336, https://doi.org/10.1186/s12964-024-01692-w.
- 42. C. Chen, T. Liu, Y. Tang, G. Luo, G. Liang, and W. He, "Epigenetic Regulation of Macrophage Polarization in Wound Healing," *Burns & Trauma* 11 (2023): tkac057, https://doi.org/10.1093/burnst/tkac057.
- 43. K. L. Singampalli, S. Balaji, X. Wang, et al., "The Role of an IL-10/Hy-aluronan Axis in Dermal Wound Healing," *Frontiers in Cell and Developmental Biology* 8 (2020): 636, https://doi.org/10.3389/fcell.2020.00636.
- 44. J. Shi, J. Li, H. Guan, et al., "Anti-Fibrotic Actions of Interleukin-10 Against Hypertrophic Scarring by Activation of PI3K/AKT and STAT3

- Signaling Pathways in Scar-Forming Fibroblasts," *PLoS One* 9, no. 5 (2014): e98228, https://doi.org/10.1371/journal.pone.0098228.
- 45. J. Henderson, M. W. J. Ferguson, and G. Terenghi, "The Reinnervation and Revascularization of Wounds Is Temporarily Altered After Treatment With Interleukin 10," *Wound Repair and Regeneration* 19, no. 2 (2011): 268–273, https://doi.org/10.1111/j.1524-475X.2011.00667.x.
- 46. D. M. Supp, "Animal Models for Studies of Keloid Scarring," *Advanced Wound Care* 8, no. 2 (2019): 77–89, https://doi.org/10.1089/wound.2018.0828.
- 47. N. Avila-Martinez, M. Gansevoort, J. Verbakel, et al., "Matrisomal Components Involved in Regenerative Wound Healing in Axolotl and Acomys: Implications for Biomaterial Development," *Biomaterials Science* 11, no. 18 (2023): 6060–6081, https://doi.org/10.1039/d3bm00835e.
- 48. L. R. Versteegden, M. Sloff, H. R. Hoogenkamp, et al., "A Salt-Based Method to Adapt Stiffness and Biodegradability of Porous Collagen Scaffolds," *RSC Advances* 9, no. 63 (2019): 36742–36750, https://doi.org/10.1039/c9ra06651a.
- 49. J. L. Balestrini, S. Chaudhry, V. Sarrazy, A. Koehler, and B. Hinz, "The Mechanical Memory of Lung Myofibroblasts," *Integrative Biology* 4, no. 4 (2012): 410–421, https://doi.org/10.1039/c2ib00149g.
- 50. J. Yin, S. Zhang, C. Yang, et al., "Mechanotransduction in Skin Wound Healing and Scar Formation: Potential Therapeutic Targets for Controlling Hypertrophic Scarring," *Frontiers in Immunology* 13 (2022): 1028410, https://doi.org/10.3389/fimmu.2022.1028410.
- 51. A. Goel and P. Shrivastava, "Post-Burn Scars and Scar Contractures," *Indian Journal of Plastic Surgery* 43, no. Suppl (2010): S63–S71, https://doi.org/10.4103/0970-0358.70724.
- 52. E. C. Soller, D. S. Tzeranis, K. Miu, P. T. C. So, and I. V. Yannas, "Common Features of Optimal Collagen Scaffolds That Disrupt Wound Contraction and Enhance Regeneration Both in Peripheral Nerves and in Skin," *Biomaterials* 33, no. 19 (2012): 4783–4791, https://doi.org/10.1016/j.biomaterials.2012.03.068.
- 53. J. C. J. Wei, G. A. Edwards, D. J. Martin, H. Huang, M. L. Crichton, and M. A. F. Kendall, "Allometric Scaling of Skin Thickness, Elasticity, Viscoelasticity to Mass for Micro-Medical Device Translation: From Mice, Rats, Rabbits, Pigs to Humans," *Scientific Reports* 7, no. 1 (2017): 15885, https://doi.org/10.1038/s41598-017-15830-7.
- 54. H. Sorg, D. J. Tilkorn, S. Hager, J. Hauser, and U. Mirastschijski, "Skin Wound Healing: An Update on the Current Knowledge and Concepts," *European Surgical Research* 58, no. 1–2 (2017): 81–94, https://doi.org/10.1159/000454919.
- 55. V. Rouet, Y. Hamma-Kourbali, E. Petit, et al., "A Synthetic Glycosaminoglycan Mimetic Binds Vascular Endothelial Growth Factor and Modulates Angiogenesis," *Journal of Biological Chemistry* 280, no. 38 (2005): 32792–32800, https://doi.org/10.1074/jbc.M504492200.
- 56. D. Papy-Garcia and P. Albanese, "Heparan Sulfate Proteoglycans as Key Regulators of the Mesenchymal Niche of Hematopoietic Stem Cells," *Glycoconjugate Journal* 34, no. 3 (2017): 377–391, https://doi.org/10.1007/s10719-017-9773-8.
- 57. V. J. Coulson-Thomas, T. F. Gesteira, J. Esko, and W. Kao, "Heparan Sulfate Regulates Hair Follicle and Sebaceous Gland Morphogenesis and Homeostasis*," *Journal of Biological Chemistry* 289, no. 36 (2014): 25211–25226, https://doi.org/10.1074/jbc.M114.572511.
- 58. D. S. Masson-Meyers, T. A. M. Andrade, G. F. Caetano, et al., "Experimental Models and Methods for Cutaneous Wound Healing Assessment," *International Journal of Experimental Pathology* 101, no. 1–2 (2020): 21–37, https://doi.org/10.1111/jep.12346.

Supporting Information

Additional supporting information can be found online in the Supporting Information section. **Data S1:** wrr70096-sup-0001-Supinfo. docx.